Protein-induced transformation of unilamellar to multilamellar vesicles triggered by a polysaccharide

Aristeidis Papagiannopoulos[1,*], Aggeliki Sklapani[1], Adél Len[2,3], Aurel Radulescu[4], Ewa Pavlova[5], Miroslav Slouf[5]

[1]Theoretical and Physical Chemistry Institute, National Hellenic Research Foundation, 48 Vassileos Constantinou Avenue, 11635 Athens, Greece.

[2]Centre for Energy Research, Konkoly-Thege str., 29-33, 1121 Budapest, Hungary

[3]University of Pécs, Faculty of Engineering and Information Technology, Boszorkány str., 2, 7624 Pécs, Hungary

[4]Jülich Centre for Neutron Science JCNS Forschungszentrum Jülich GmbH, Outstation at Heinz Maier-Leibnitz Zentrum (MLZ), Lichtenbergstraße 1, 85747 Garching, Germany.

[5]Institute of Macromolecular Chemistry, Czech Academy of Sciences, Heyrovskeho nam.. 2, 16206 Prague, Czech Republic

Email: apapagiannopoulos@eie.gr

Abstract

We report on the morphological transitions of didodecyldimethylammonium bromide (DDAB) cationic vesicles and hybrid DDAB/hyaluronic acid (HA) vesicles upon addition of BSA at pH 7 where BSA is overall negatively charged. Small angle neutron scattering (SANS) is used to extract the size distributions of the nanovesicles, the thickness of the DDAB bilayers and their lamellarity. Although the HA-decorated DDAB vesicles contain the negatively charged polysaccharide the interaction with BSA appears to be more intense in comparison to bare vesicles. Characteristic peaks in the SANS patterns indicate the presence of multilamellar interfaces while the formation of multilamellar vesicles induced by BSA depends on the amount of added HA. Consequently, higher lamellarities are observed at higher BSA contents. This work demonstrates a simple methodology to tune the encapsulation of globular proteins in vesicular nanoassemblies by

affecting their lamellarity and has direct implications on the application of vesicles and liposomes in protein delivery.

Keywords

didodecyldimethylammonium bromide; bovine serum albumin; hyaluronic acid; small angle neutron scattering

Introduction

Self-assembled vesicular nanocarriers based on surfactants and lipids are very attractive for the encapsulation and delivery of bioactive compounds that include genetic material, molecular drugs, toxins and enzymes (Salim et al. 2014). Incorporation of polysaccharides to vesicular nanostructures increases their biocompatibility, targeting ability and structural stability. Polysaccharides have been used as coatings for soybean phospholipid liposomes to control and optimize the release and antioxidant activity of the encapsulated quercetin (Román-Aguirre et al. 2020). The surface charge, stability in saliva and mucoadhesion of liposomes from various lipids were tested by coating by several polysaccharides by electrostatic deposition (Pistone et al. 2017). Soy bean phospholipid/cholesterol liposome nanocarriers for the model antigen olvabumin were enriched by *Lycium barbarum* polysaccharides to effectively improve cellular immune responses (Bo et al. 2017). Alternating layers of xanthan and glactomannan were deposited on dioctadecyldimethylammonium bromide (DODAB) liposomes and successfully improved the release profile of epidermal growth factor (Kaminski et al. 2016). Transferrin-functionalized vesicles mixed with dextran sulfate/doxorubicin and alginate/cisplatin complexes were designed for receptor-mediated endocytic uptake by cancer cells (Ruttala et al. 2017).

Self-assemblies of vesicles and biomacromolecules such as DNA and proteins are inherently biocompatible and have great potential as drug nanocarriers (Liu et al. 2014). Globular proteins interact strongly with lipid bilayers causing structural rearrangements e.g., to cell membranes (Ruggeri et al. 2013). The number of bilayers in liposomal formulations i.e. lamellarity is a key factor in applications that involve encapsulation, release and cellular uptake (van der Koog et al. 2022). Nanosized multilamellar vesicles were proven efficient for the *in vivo* delivery of antigens and the enhancement of their immunogenicity (Rodrigues-Jesus et al. 2019). Encapsulation of pneumococcal polysaccharides and Diphtheria CRM197 protein in multilayer vesicles with noncovalent bonds was applied to produce vaccines against pneumococcal disease (Nayerhoda et al. 2021). The interaction of the epidermal growth factor with cationic unilamellar lipid vesicles led to a transformation of the vesicles to multilamellar ones and increased the protein loading efficiency significantly (Koo et al. 2021). The interaction of bovine serum albumin (BSA) with the oppositely charged vesicles of didodecyldimethylammonium bromide (DDAB) has been reported to be greatly enhanced by the preadsorption of the anionic hyaluronic acid on the vesicles (Papagiannopoulos 2018). Therefore, the interplay between polysaccharides and proteins in lipid or surfactant lamellae interfaces has great potential for advanced protein nanocarriers of high and tunable loading capacity.

In this work we investigated the morphological rearrangements in the cationic DDAB vesicles either bare or decorated by HA induced by the model protein BSA. We used small angle neutron scattering (SANS) to quantify the size distribution, shape, bilayer structure and lamellarity transitions in the vesicles. The experiments included measurements on the binary mixtures (DDAB/HA and DDAB/BSA). SANS data were analyzed by the superposition of the analytical form factors of polydisperse spherical vesicles of different lamellarities. Bayesian inference was

used to quantify the interdependencies between the fitting parameters and the parameter uncertainties. This study illustrates how the interaction of proteins with complex surfactant/polysaccharide vesicular interfaces can be used to tailor-make their lamellarity and therefore the loaded protein amount.

2. Materials and Methods

2.1 Materials and sample preparation

Didodecyldimethylammonium bromide (DDAB) was purchased from Fluka, hyaluronic acid (HA) in the sodium salt form with M = 5000 $gmol^{-1}$ (PDI ~ 1.5) was a kind gift from Uni-Pharma (Greece) and bovine serum albumin (BSA) was obtained from Sigma-Aldrich. Stock solutions of the separate components in D_2O (0.01 M NaCl and pH 7) i.e., DDAB (10 $mgml^{-1}$), HA (3 $mgml^{-1}$) and BSA (30 $mgml^{-1}$) were prepared and kept overnight at 4 °C to dissolve and equilibrate. The final mass concentrations in the samples were achieved by mixing proper volumes of D_2O (0.01 M NaCl and pH 7) with stock solutions under gentle stirring. In the dual mixtures, volumes of the DDAB stock solutions were added to D_2O first and the ones of HA or BSA afterwards. In the ternary mixtures HA solution was added before BSA solution. All experiments were performed at room temperature. A list of the samples that were studied in this work is provided in Table 1.

Table 1. Samples and concentrations of the individual components in $mgml^{-1}$.

Sample	1	2	3	4	5	6	7	8	9	10	11	12	13	14
DDAB	3	3	3	3	3	3	3	3	3	3	3	3	3	3
HA	-	0.1	0.2	0.3	0.4	-	-	0.1	0.1	0.3	0.3	0.4	0.4	0.4
BSA	-	-	-	-	-	0.5	1.5	0.5	1.5	0.5	1.5	0.5	1.5	2.0

2.2 SANS experiments

The SANS diffractometer Yellow Submarine (Budapest Neutron Centre) was used for SANS measurements (Len and Almásy 2019, Almásy 2021). Three different sample-detector distance/wavelength (λ) configurations were used to collect scattered neutrons i.e., 5.26 m/12 Å, 5.26 m/4.94 Å and 1.16 m/4.94 Å. Corrections were made for contributions of the empty cell and the solvent and the detector efficiency was taken into account. The scattered intensities were set to absolute scale by measuring an H_2O sample. Azimuthal integration of the collected isotropic 2-D raw data resulted in the 1-D scattered intensity $I(q)$ data, where q is the scattering wave vector. Convolution by a Gaussian function (Barker and Pedersen 1995) was performed on the theoretical SANS profiles $I^{th}(q)$ to take instrumental resolution function $\Delta q(q)$ into account (Radulescu et al. 2015) i.e.

$I^{conv}(q) = \frac{1}{\sqrt{2\pi}\Delta q(q)} \int_{-\infty}^{+\infty} dq' \cdot exp\left(-\left(\frac{q'-q}{\sqrt{2}\Delta q(q)}\right)^2\right) \cdot I^{th}(q')$. In this work $\frac{\Delta q(q)}{q} \approx \frac{\Delta\lambda}{\lambda} = 0.2$ was applied.

2.3 SANS model

The experimental data from SANS were fitted with the form factors of multilamellar polydisperse spherical vesicles (Papagiannopoulos et al. 2021*a*). The scattered intensity from N separate populations of vesicles of different size and lamellarity is written as in equation 1.

$$I(q) = \sum_{i=1}^{N} N_i \cdot |A_i(q)|^2 \cdot S_i(q) \qquad (1)$$

The number concentrations (N_i) of uni-lamellar ($i = 1$), bi-lamellar ($i = 2$) etc vesicles define the relative contributions in the superposition of the vesicular form factors. The scattering amplitude $A_i(q)$ of a single vesicle consisting of i concentric layers (shells) is defined in equation 2.

$$A_i(q) = \sum_{j=1}^{i} A_{shell}\left(q, B, R_j, R_j + d\right) \quad (2)$$

Where R_j is the internal radius of the vesicle with $R_j = R_{j-1} + d + t$, for $j > 1$, d the thickness of the shells and t the radial distance between successive shells within the vesicle. The scattering amplitude of a spherical shell is shown in equation 3.

$$A_{shell}(q, B, R, R') = \frac{4\pi B}{q^3} \cdot \left((sinqR' - qR'cosqR') - (sinqR - qRcosqR)\right) \quad (3)$$

The contrast factor B is provided by equation 4.

$$B = \rho_{DDAB} - \rho_{D_2O} \quad (4)$$

The neutron scattering length densities (NSLD) of the solvent and DDAB were $\rho_{D2O} = 6.4 \cdot 10^{-6}\text{Å}^{-2}$ and $\rho_{DDAB} = -0.25 \cdot 10^{-6}\text{Å}^{-2}$ (Eastoe et al. 1997, Griffin et al. 2016) respectively. In all cases the lamellar bilayers were modelled as uniform spherical shells with NSLD the one of DDAB.

The Debye factors $S_i(q)$ (equation 1) were used to fit the upturn at low q in the case of unilamellar vesicles and are provided by equation 5. This is the scattering contribution from the formation of vesicle dimers with centre-to-centre distance D_i (Pedersen 1997, Stovgaard et al. 2010). A prefactor n_i is applied to define the extent of dimer formation. It equals 1 when all vesicles are in pairs and 0 when they are all in unimeric state. Therefore, n_i represents the ratio of the number of vesicles that take part in dimers over the total number of vesicles.

$$S_i(q, n_i, D_i) = 1 + n_i \cdot \frac{sinqD_i}{qD_i} \qquad (5)$$

The size polydispersity of the vesicles was taken into account by a Schultz distribution for the vesicular internal radii (Kotlarchyk et al. 1988). The scattered intensity from the polydisperse sample was expressed as $I^{poly}(q;R) = \frac{\left(\frac{z+1}{R}\right)^{z+1}}{\Gamma(z+1)} \int_0^{+\infty} dr \cdot r^z \cdot exp\left(-\frac{z+1}{R} \cdot r\right) \cdot I^{conv}(q;r)$ where R was the mean internal radius. The polydispersity index is defined as $PDI = (z+1)^{-1/2}$ while $PDI = \frac{\sigma_R}{R}$ with σ_R the root-mean-square deviation from the mean radius.

2.4 SANS data optimization and error analysis

A Monte Carlo simulated annealing minimization scheme was implemented for the data optimization (Vanderbilt and Louie 1984). In the fitting procedure the calculation of $I^{conv}(q)$ and the minimization of the sum of the weighted square differences $\chi^2 = \sum_{i=1}^{N} \left(\frac{I^{conv}(P;q_i) - I^{exp}(q_i)}{\delta I^{exp}(q_i)}\right)^2$ between N theoretical and experimental intensities were performed. P was the set of the optimization parameters $\{P_i\}$, $I^{exp}(q_i)$ was the experimentally obtained intensity and $\delta I^{exp}(q_i)$ its uncertainty at $q = q_i$. A custom-made code in MATLAB was used for the calculations. The Markov Chain Monte Carlo (MCMC) algorithm of Goodman and Weare (Goodman and Weare 2010) was applied to acquire the posterior distributions of the fitted parameters. The Bayesian analysis (Winslow et al. 2019) was based on 100 Markov chains of 1000 steps each that were followed after disregarding the period of the convergence of the simulated annealing process (burn-in period). Corner plots (forthcoming) were used in order to visualize the pair-wise dependence between the fitted parameters. The correlation coefficients between fitted parameters were calculated by $r(P_i, P_j) = \frac{1}{M-1} \sum_{k=1}^{M} \left(\frac{P_i^k - \langle P_i \rangle}{\delta P_i}\right)\left(\frac{P_j^k - \langle P_j \rangle}{\delta P_j}\right)$ where $\langle P_i \rangle$ and δP_i are the mean and

158 standard deviation of P_i respectively over the space of the M pairs of parameters instances P_i^k and
159 P_j^k.

160 **2.5 Cryo-transmission electron microscopy**

161 Cryogenic transmission electron microscopy (cryo-TEM) images were obtained with a Tecnai G2
162 Spirit Twin 12 microscope (FEI, Czech Republic) equipped with a cryo-attachment (Gatan, CA,
163 USA). The samples for cryo-TEM were prepared as follows: 3 μL of the sample solution were
164 dropped onto an electron microscopy grid covered with a holey carbon supporting film (Electron
165 Microscopy Science), which was hydrophilized just before the experiment by means of glow
166 discharge (Expanded Plasma Cleaner, Harrick Plasma, USA). The excess of the solution was
167 removed by blotting (Whatman no. 1 filter paper) for 1 s, and the grid was plunged into liquid
168 ethane held at 181 °C. The frozen sample was immediately inserted in the cryo-holder, transferred
169 into the TEM microscope and observed at -173 °C using bright field imaging at the accelerating
170 voltage of 120 kV.

171 **3. Results and discussion**

172 SANS customarily resolves spatial correlations in the range 1-100 nm. The results on the DDAB
173 solutions are shown in Fig. 1. It is evident that the form factor from these solutions is reminiscent
174 of the one from spherical vesicles with a characteristic shoulder (between 10^{-2} and $2\text{x}10^{-2}$ Å^{-1}) (Fig.
175 1a) and a steep decrease at higher q (between $1.8\text{x}10^{-1}$ and $2\text{x}10^{-1}$ Å^{-1}) (Papagiannopoulos et al.
176 2021*a*). The characteristic power-law behavior $I{\sim}q^{-2}$ that was to a good degree followed at
177 intermediate q (Fig. 1b) strongly supported the presence of thin lamella sheets i.e., the presence of
178 the DDAB bilayers in the solutions. Indeed, the data from pure DDAB (sample 1) were fitted by
179 equation 1. A detailed Bayesian analysis on the fitted parameters is presented in the Supporting

Information. The interdependencies of the fitted parameters for representative data sets are presented in color plots in Fig. S1. The correlation coefficients are presented in Tables S1 and S2 for the representative data sets.

For sample 1 only the term $i = 1$ in equation 1 was used, showing that only unilamellar vesicles were present. The data from the DDAB vesicles with added HA were quantitatively similar with the ones of pure DDAB (Fig. 1a) and were fitted with the same model as sample 1 (Fig. 1b). The low-q upturn was adequately compensated by the Debye structure factor $S_i(q)$ showing that some aggregation of the vesicles takes place. This upturn however does not interfere with the scattering at intermediate and high q where the shape of the spherical vesicles is determined. Interestingly, this aggregation becomes stronger as more HA is added to the solution. This shows that the anionic polysaccharide enhances the bridging interactions between the vesicles as it is attracted from the positive charge of DDAB.

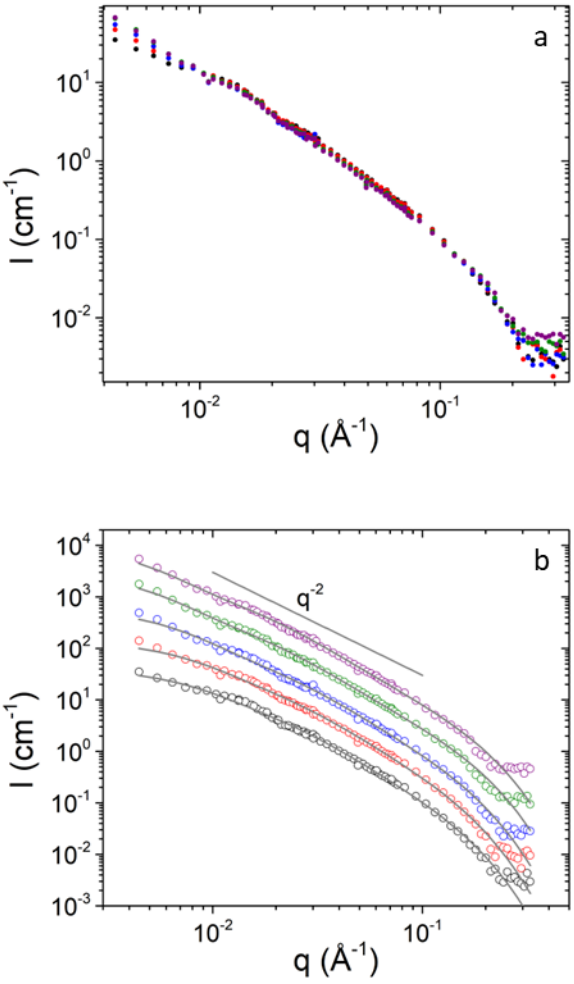

192

193 Figure 1. SANS data from DDAB and HA-decorated DDAB vesicles. Sample 1 (black), 2 (red), 3
194 (blue), 4 (green) and 5 (magenta). (a) SANS intensities. (b) SANS intensities fitted by the
195 unilamellar vesicles model. Lines show best fits. Data sets are separated by factors of 3 from each
196 other for clarity.

197

198 Table 2. SANS parameters for DDAB vesicles upon addition of HA from fitting with the
199 unilamellar vesicles model.

Parameter\Sample	1	2	3	4	5	$\delta P_i/P_i$ (%)*

$N\left(10^{-8}\text{Å}^{-3}\right)$	0.886	0.876	0.862	0.878	0.893	2.9
$R(nm)$	1.76	1.75	1.86	2.40	2.52	2.1
$d\ (nm)$	1.78	1.75	1.63	1.50	1.43	1.7
n	1.84	2.15	2.82	2.47	2.53	9.6
$D\ (nm)$	7.55	7.70	9.24	11.65	12.52	4.4
$d_{ves}\ (nm)$	7.08	7.00	6.98	7.80	7.90	1.2

200 *uncertainties are extracted by Bayesian analysis (see Supplementary Material)

201 The thickness of the DDAB bilayers was about 1.8 nm and decreased to 1.4 nm for high HA
202 contents. This value is compatible with previous studies on DDAB bilayers in microemusions
203 (Eastoe et al. 1997) and on quartz surfaces (Blom et al. 2007). The decrease in thickness upon
204 addition of HA shows a possible change in the packing of the double-tailed surfactants within the
205 interfaces which was possibly induced by the attractive interactions with the polysaccharide
206 chains. A PDI of 0.75-0.85 was used in all cases revealing a very broad distribution of vesicular
207 sizes. For example, in pure DDAB roughly 90% of the vesicles have diameters between 4 and 13
208 nm. Previous TEM studies have shown that in DDAB solutions of concentrations of 5 $mgml^{-1}$
209 unilamellar vesicles of sizes in the order of 10 nm or smaller were formed (Regev and Khan 1994).
210 High values of polydispersity have been reported for dioleoylphosphatidylcholine (DOPC)-
211 dioleoylphosphatidylethanolamine (DOPE) vesicles (PDI~0.6) (Komorowski et al. 2018) and in
212 our previous work on dipalmitoylphosphatidylcholine (DPPC) unilamellar vesicles (PDI~0.7-0.8)
213 (Papagiannopoulos et al. 2021*b*). Schultz distributions naturally reproduce populations with high
214 positive skewness (Helfrich 1986). In theoretical studies where nonlinear elasticity contributions
215 were taken into account and for bending stiffnesses about 5-10 k_BT highly asymmetric
216 distributions were predicted (Huang Changjin et al. 2017). Remarkably diameters of vesicles
217 showed a sharp increase above the minimum value which was in the order or lower than 10 nm
218 and an extended tail to large diameters above 40-50 nm. An increase in the bending stiffness gave
219 rise to a shift of the distribution maximum to higher values and made the shape of the distribution

more symmetric. In the case of DDAB vesicles the internal radius increased from roughly 1.8 to 2.5 nm and the overall diameter from about 7 to 8 nm upon addition of HA (Table 2). It could be assumed that HA chains increase the rigidity of the vesicular interfaces by their mutual steric and electrostatic repulsions. Similar effects have been reported in anionic vesicles with adsorbed chitosan (Lee et al. 2006) and DPPC vesicles with cationic polyoxazoline polyelectrolytes (Papagiannopoulos et al. 2021*a*). In addition, the bridging effects caused by HA became stronger as more polysaccharide was added and the prefactor n increased. Regarding the separation distance D in the aggregated pairs it fairly agreed with the diameter of the vesicles d_{ves} at low HA contents (samples 1 and 2) however it was higher at high HA contents (samples 3, 4 and 5). This may indicate that the higher density of HA monomers in the region between aggregated vesicles leads to higher intervesicular distances. The number density of vesicles N appeared fairly independent on HA content (Table 2). This showed that HA did not cause reassociation of the DDAB nanovesicles that were already self-assembled in pure DDAB solutions. A schematic illustration of the morphological transitions upon addition of HA on the DDAB vesicles is presented in Scheme 1.

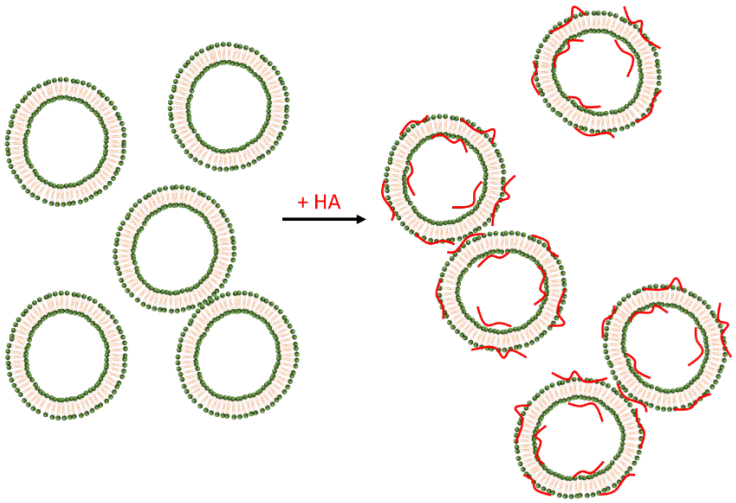

Scheme 1. Schematic diagram of the interaction of HA with the DDAB vesicles.

The results on the evolution of the radius and diameter of the vesicles upon HA addition can be discussed in terms of the critical packing parameter. This is defined by p = v/al, where v is the volume of the hydrophobic segment, a is the hydrophilic headgroup area and l is the hydrophobic chain length (Kunz et al. 2009). This dimensionless parameter is connected to the expected morphology i.e. spherical micelles, worm-like cylinders and vesicles are predicted for $p<1/3$, $1/3<p<1/2$ and $1/2<p<1$ respectively. Indeed, the double-chained cationic surfactant DDAB has a roughly cylindrical shape and a packing parameter at about 0.62 that favors bilayer structures in water (Marques et al. 2003). Therefore, an increase in the mean vesicular radius may indicate an increase of the packing parameter. Apparently, the attractive interaction of DDAB cationic head groups with hyaluronic acid leads to a closer packing of the head groups resulting to a smaller hydrophilic head group area and a higher effective packing parameter (Sun et al. 2019).

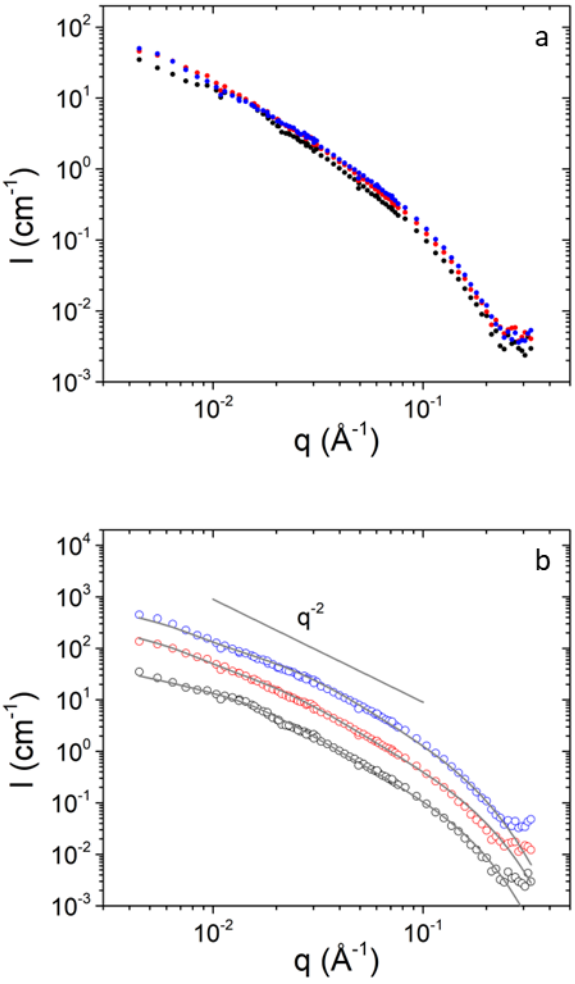

Figure 2. SANS data from pure DDAB vesicles and DDAB vesicles with added BSA. Sample 1 (black), 6 (red) and 7 (blue). (a) SANS intensities. (b) SANS intensities fitted by the unilamellar vesicles model. Lines show best fits. Data sets are separated by factors of 3 from each other for clarity.

The SANS profiles from the solutions of DDAB vesicles with added BSA are shown in Fig. 2. Comparing with the data from pure DDAB it was evident that there was an increase in the low-q upturn upon addition of BSA. This means that the protein enhanced the bridging effects. As the

overall charge of BSA at pH 7 is negative the protein was attracted by the positive surfactant heads. The factor n of the pair structure factor increased gradually from the pure vesicles (n=1.84) to sample 6 (n=1.89) and sample 7 (n=1.98) although within experimental error (Table 3). The vesicular internal radius and diameter were not different than the ones of pure DDAB (Tables 2 and 3). Evidence of the presence of BSA on the surface of the vesicles was given by the increased separation distance D which was about 11 nm. The number concentration of vesicles was higher than in the case of pure DDAB showing that more vesicles were formed in the presence of BSA. The thickness of the bilayers remained the same (within experimental error) for low protein content (1.7 nm) and slightly increased for higher protein content (1.9 nm). A schematic illustration of the morphological transitions upon addition of BSA on the DDAB vesicles is presented in Scheme 2.

Table 3. SANS parameters for DDAB vesicles upon addition of BSA from fitting with the unilamellar vesicles model.

Parameter\Sample	6	7	$\delta P_i/P_i$ (%)*
$N\left(10^{-8}\text{Å}^{-3}\right)$	0.998	1.085	2.9
$R(nm)$	2.22	1.88	2.1
$d\ (nm)$	1.72	1.88	1.7
n	1.89	1.98	9.6
$D\ (nm)$	11.05	11.18	4.4
$d_{ves}\ (nm)$	7.88	7.52	1.2

*uncertainties are extracted by Bayesian analysis (see Supplementary Material)

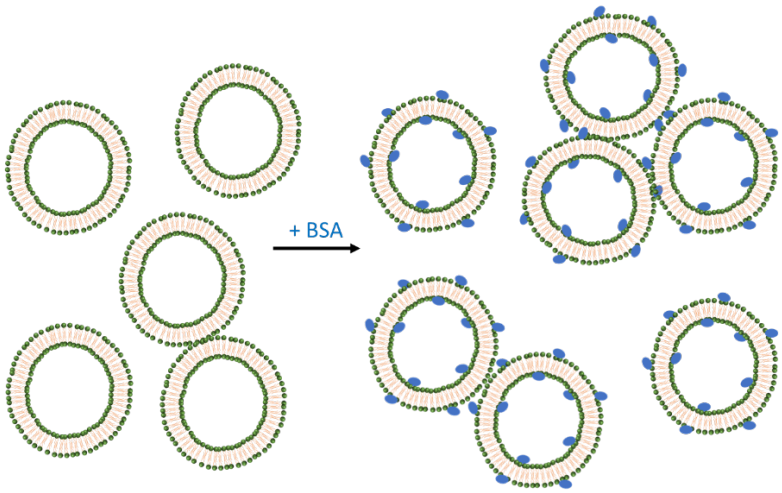

Scheme 2. Schematic diagram of the interaction of BSA with the DDAB vesicles.

Addition of BSA to the vesicles with preadsorbed HA of low concentration (0.1 $mgml^{-1}$) i.e. samples 8 and 9 caused similar effects as in the case of pure DDAB vesicles (Fig. 3) as the SANS data could still be fitted by the unilamellar model (Table 4). The number density of vesicles (N≈1.2) increased in comparison to vesicles either in the presence of HA (N≈0.9) or in the presence of BSA (N≈1.0). This revealed a stronger interaction of BSA with the HA-decorated vesicles in comparison to pure vesicles. Consequently, this interaction was capable of altering the self-assembly of DDAB vesicles. The increase in N maybe explained by the reassembly of DDAB molecules and HA chains in a new rearranged bilayer structure that included BSA and led to a higher number of vesicles. The thickness of the bilayers (d≈1.6 nm) was a little lower than the one of pure DDAB vesicles (d≈1.7-1.8 nm). The internal radius of the vesicles was also lower than the one of pure DDAB vesicles i.e. 1.3 nm in comparison to 1.7-1.8 nm possibly because of a drastic change in packing of the molecules within the bilayers in the presence of BSA. Possibly the steric effects of BSA cause a decrease of the effective packing parameter p (by increasing the head group

area) and a trend towards higher curvatures. The percentage of aggregated vesicles was relatively high showing that bridging effects were stronger when BSA was present. This is a sign that when BSA interacted with the mixed cationic (DDAB)/ anionic (HA) membrane it had more intense effect than when it interacted with the pure cationic interface. This is a counterintuitive result as it would be expected for BSA to interact more strongly with the oppositely charged membrane than with the mixed positive/negative membrane. We have seen an effect of this nature in an earlier study of this system at higher length scales using static light scattering (Papagiannopoulos 2018). The interaction was revealed by significant changes in the mass of the aggregated vesicles. It has to be noted however, that in the previous study the particles observed were considered to be vesicles and had radii in the order of 100 nm. As in the current study it was revealed that the vesicular structure was smaller than 100 nm, the particles observed with light scattering should be rather considered as clusters of vesicles.

BSA has been shown to bind more strongly to the mixed interface even when this has a net negative sign as has been quantified by zeta potential measurements (Papagiannopoulos 2018). Protein surface patches with net charge of the same sign to that of biopolymers (Comert et al. 2016) or synthetic polymers (Becker et al. 2012) may still experience attractive forces when the protein surface patch is anisotropic. Similarly in interfaces that contain polyelectrolytes proteins maybe attracted by the polyelectrolyte layer. At pH 7 BSA has a net charge of about -12 and a strong dipole moment [34]. Therefore, it is very possible that the complex DDAB/HA interface creates an electrostatic landscape that accommodates BSA molecules more effectively by the aid of both its negative and positive charge than it would be on a uniformly positive interface of the pure DDAB vesicles. From the SANS results (Table 2 and relevant discussion) and our previous light scattering work (Papagiannopoulos 2018) the interaction of BSA molecules with DDAB is proved.

Interaction of BSA and HA at pH 7 is expected to be very weak if not negligible as the two macromolecules are of the same net charge (Lenormand and Vincent 2011). Hence, the increased attraction on the DDAB/HA interface is a unique feature of this complex interface.

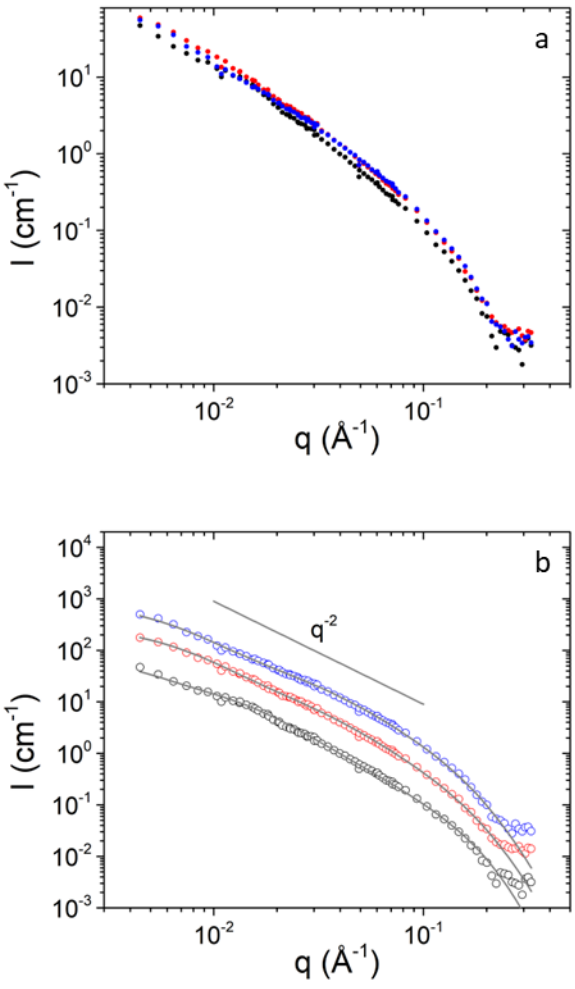

Figure 3. SANS data from HA-decorated DDAB vesicles (sample 2, black) and HA-decorated DDAB vesicles with added BSA (sample 8, red and 9, blue) with concentration of HA at 0.1 mgml^{-1}. (a) SANS intensities. (b) SANS intensities fitted by the unilamellar vesicles model. Lines show best fits. Data sets are separated by factors of 3 from each other for clarity.

Table 4. SANS parameters for HA-decorated DDAB vesicles upon addition of BSA and vesicular models used. “Uni” stands for unilamellar, “tetra” for tetralamellar and “nova” for novalamellar vesicles.

Parameter\Sample	8	9	10	11	12	13	14	$\delta P_i/P_i$ (%)*
Model	uni	uni	uni+tetra	uni+tetra	uni+tetra	uni+hexa	uni+nona	
$N_{\text{uni}}\left(10^{-8}\text{Å}^{-3}\right)$	1.164	1.272	0.878	0.932	0.872	1.089	0.981	4.3
$R_{\text{uni}}(nm)$	1.37	1.27	2.39	2.19	2.34	2.45	2.26	1.9
$d\ (nm)$	1.59	1.65	1.73	1.71	1.74	1.40	1.30	2.1
n_{uni}	5.78	5.93	0.24	0.26	0.29	0.35	0.29	11.9
$D_{\text{uni}}\ (nm)$	9.05	10.38	6.52	7.20	6.19	9.29	7.44	6.4
$d_{ves,\text{uni}}\ (nm)$	5.92	5.84	8.24	7.80	8.16	7.70	7.12	1.2
$N_{\text{multi}}\left(10^{-8}\text{Å}^{-3}\right)$	-	-	$6.32\text{x}10^{-3}$	$7.93\text{x}10^{-3}$	$6.52\text{x}10^{-3}$	$4.47\text{x}10^{-3}$	$3.83\text{x}10^{-3}$	8.6
$R_{\text{multi}}(nm)$	-	-	14	16.2	12.8	19.9	17.6	12.5
$t\ (nm)$	-	-	6.16	7.52	6.21	8.25	8.29	8.8
$d_{ves,\text{multi}}\ (nm)$	-	-	78.8	91.2	76.78	139.1	191.24	9.8
$d-spacing\ (nm)$	-	-	7.89	9.23	7.95	9.65	9.59	8.9

*uncertainties are extracted by Bayesian analysis (see Supplementary Material)

In Fig. 4 the SANS results from the interaction of BSA with the HA-decorated vesicles at 0.3 mgml^{-1} HA are shown. At this intermediate HA content it was evident that multilamellar vesicles appeared in solution as indicated by the weak peaks at about $7\text{x}10^{-2}$ and $1.4\text{x}10^{-1}$ Å^{-1}. The data from samples 10 and 11 were fitted by the combination of the unilamellar model and a tetralamellar model. There are two mechanisms proposed for the stabilization of unilamellar mechanisms against the formation of vesicles with higher lamellarity. At low bending constants (~k_BT) Hekfrich undulations destabilize the formation of concentric bilayers by an effective repulsive potential between bilayers. In more rigid bilayers a spontaneous curvature is energetically preferable excluding bilayers of different radii (Jung H. T. et al. 2001). On the other hand, hydrophobic effects stabilize multilayered vesicles by hydrophobic interactions. This has been

339 reported for DPPC vesicles with incorporated poly(2-methyl-2-oxazoline)-grad-poly(2-phenyl-2-
340 oxazoline) (MPOx) amphiphilic copolymers (Papagiannopoulos et al. 2021*a*) and for mixed
341 cationic cetyl trimethylammonium tosylate (CTAT)/anionic sodium dodecyl benzene sulfonate
342 (SDBS) unilamellar vesicles with the addition of hydrophobically modified chitosan (Lee et al.
343 2006). In the current work the electrostatic attraction of BSA with the bilayer interfaces effectively
344 glues together successive lamellae layers and leads to multilayered formulations.

345 The number density of unilamellar vesicles is similar to the one in pure DDAB however there is
346 also a number density of tetralamellar vesicles (6-7x10^{-11} $Å^{-3}$) (Table 4). The internal radius R of
347 unilamellar vesicles (~2.2-2.3 nm) is higher than the one of the pure DDAB vesicles (Table 2) and
348 similar to the one of the DDAB vesicles with low amount of added BSA (Table 3). The value of n
349 is fairly low possibly because scattered intensity at low q is greatly enhanced by the presence of
350 multilamellar vesicles. The tetralamellar vesicles have an internal radius 14-16 nm and an
351 interlamellar distance t between 6 and 8 nm. This is in fair agreement with the geometrical features
352 of BSA globules which can be considered as prolate ellipsoids with major axis at about 4.5 nm
353 and eccentricity at 0.27 (Mehan et al. 2013, Papagiannopoulos et al. 2017). Therefore, it can be
354 assumed that BSA globules could fit the interlamellar spaces as a single or a double layer
355 depending on their orientation. The size of the tetralamellar vesicles could reach 80-90 nm. The
356 characteristic $d_{spacing}$ is the thickness of a repetitive lamellae including the interlamellar spacing
357 i.e. $d_{spacing} = d + t$. Using Bragg's law $d_{spacing}$ is derived from the values of q at the first and
358 second intensity maximum i.e. $d_{spacing} = \frac{2\pi}{q_1^*} = 2\frac{2\pi}{q_2^*}$. The data of Fig. 4 result to a $d_{spacing}$ at 8-9 nm
359 which is compatible with the values of Table 4. A schematic illustration of the effect of BSA
360 addition on HA-decorated vesicles for HA concentration at 0.3 $mgml^{-1}$ is presented in Scheme 3.

361

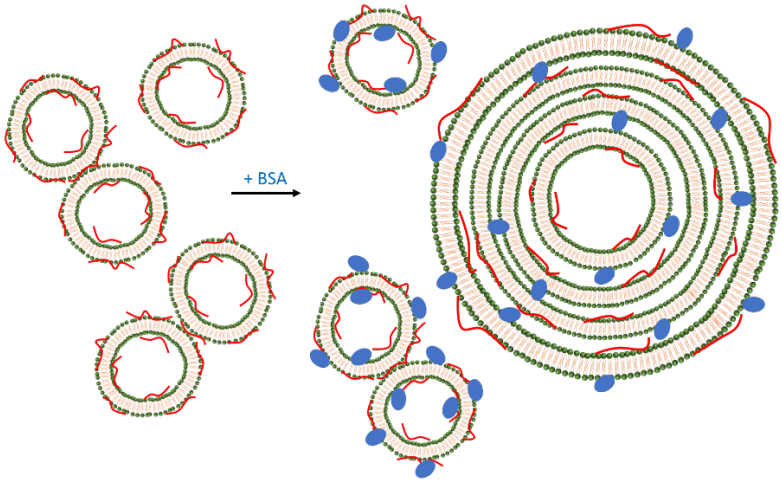

Scheme 3. Schematic diagram of the interaction of BSA with the HA-decorated DDAB vesicles at 0.3 $mgml^{-1}$ HA.

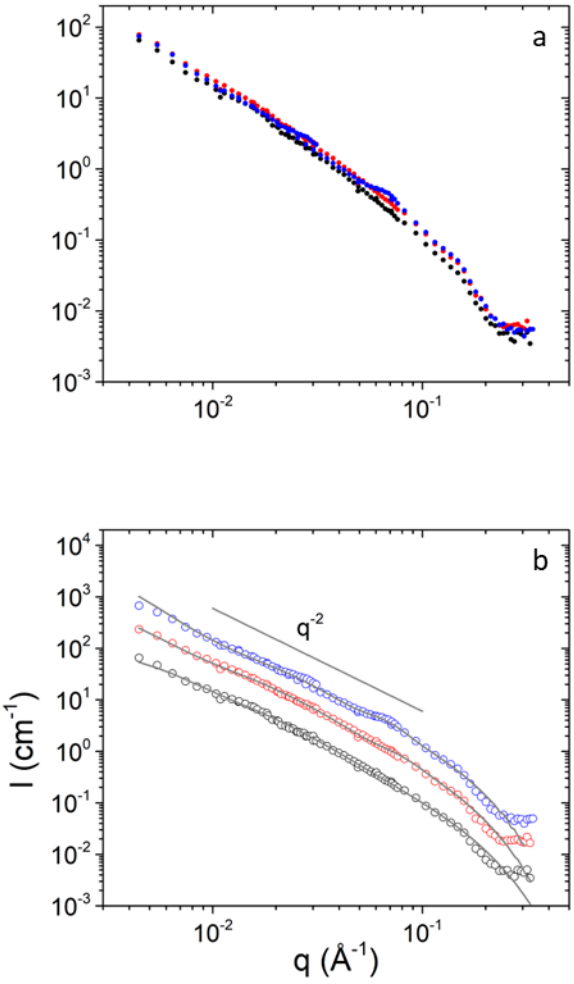

368

369 Figure 4. SANS data from HA-decorated DDAB vesicles (sample 4, black) and HA-decorated
370 DDAB vesicles with added BSA (sample 10, red and 11, blue) with concentration of HA at 0.3
371 mgml^{-1}. (a) SANS intensities. (b) SANS intensities fitted by the unilamellar vesicles model. Lines
372 show best fits. Data sets are separated by factors of 3 from each other for clarity.

373

374 At HA-decorated DDAB vesicles with higher amount of HA (0.4 mgml^{-1}) the presence of
375 characteristic peaks in the SANS intensity is even more pronounced (Fig. 5). The data are fitted
376 by combinations of unilamellar vesicles and multilamellar vesicles. The characteristics of the

unilamellar vesicles are similar to the ones of the unilamellar vesicles at 0.3 $mgml^{-1}$ (samples 10 and 11). The only exceptions are the thickness of the bilayer which is closer to the one of DDAB/HA vesicles at 0.4 $mgml^{-1}$ HA in the absence of BSA. It is notable that in the case of the increased amount of added HA i.e. 0.4 $mgml^{-1}$ the interaction with BSA is stronger than at 0.3 $mgml^{-1}$ and the resulting multilamellar vesicles have higher lamellarities. For sample 13 vesicles with 6 bilayers and for sample 14 vesicles with 9 bilayers appear. This is a remarkable result which shows great potential for protein nanodelivery. The added amount of polysaccharide can be used to tune the vesicular lamellarity and the amount of protein that is encapsulated in multilayers of the vesicles. The overall size of the DDAB/HA/BSA vesicles reaches values of the order 140-190 nm. The interlamellar distances are about 8-9 nm which is somewhat higher than the one at lower HA contents however still compatible with the BSA size. The $d_{spacing}$ is also compatible with the positions of the intensity peaks.

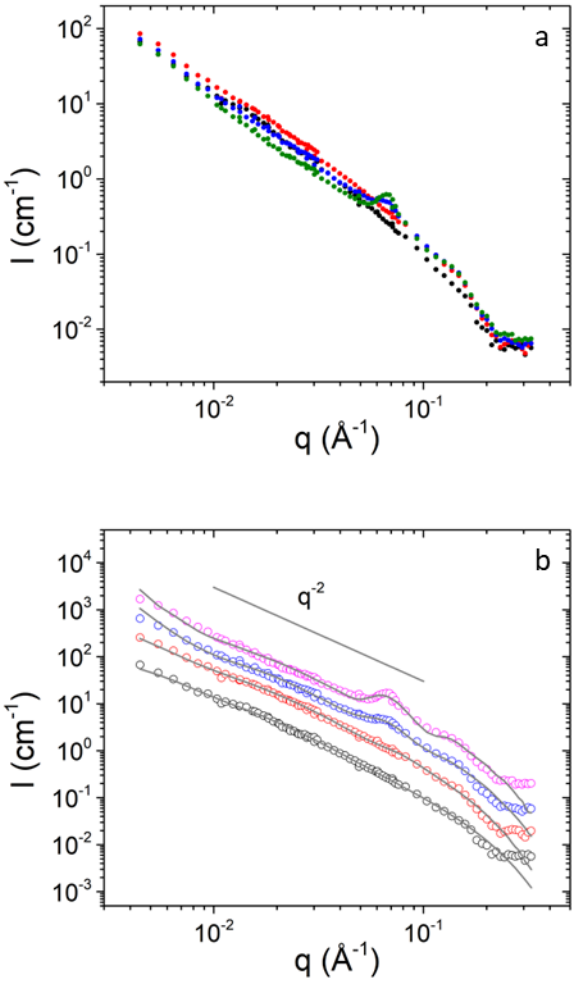

Figure 5. SANS data from HA-decorated DDAB vesicles (sample 5, black) and HA-decorated DDAB vesicles with added BSA (sample 12, red, 13, blue and 14, magenta) with concentration of HA at 0.4 mgml^{-1}. (a) SANS intensities. (b) SANS intensities fitted by the unilamellar vesicles model. Lines show best fits. Data sets are separated by factors of 3 from each other for clarity.

Cryo-TEM results corroborate with the findings of SANS. In the absence of HA the vesicles with added BSA appear mainly with single lamellae (Fig. S2a). However, there are cases of vesicles with double lamellae which apparently arise from the coalescence of two unilamellar vesicles. The

size of the vesicles is higher in comparison to SANS. These facts may be connected to instabilities of the samples as cryo-TEM experiments were performed several days after the sample preparation. The appearance of multilamellar vesicles in the case of HA-decorated vesicles at high amounts of added BSA is illustrated in Fig. S2b. In addition, some signs of impurities appear possibly coming from the BSA and HA powders that was used as received. The higher concentration of BSA and HA in the solutions of samples 12, 13, and 14 resulted in a higher viscosity of the system and, consequently, in a higher thickness of the amorphous ice layer during the sample preparation for cryo-TEM. This led to somewhat lower contrast in Fig. S2b and in all other micrographs showing the samples 12, 13, and 14.

4. Conclusions

This investigation presents the ability of DDAB vesicles to transform from unilamellar to multilamellar vesicles by addition of a globular protein depending on the amount of an added anionic polysaccharide. SANS experiments efficiently characterized the size distribution and number density of vesicles in pure DDAB solutions, in DDAB/HA and DDAB/BSA mixtures. When DDAB vesicles were decorated by HA at low concentrations, only unilamellar vesicles were found in solution as in the case of the binary mixtures even upon addition of BSA. At intermediate concentrations of added HA the addition of BSA led to the creation of tetralamellar vesicles. At high HA content BSA created tetralamellar, hexalamellar and nonalamellar vesicles as its concentration increases. The SANS data modelling was supported by Bayesian analysis to explore the interdependencies between the fitting parameters and to justify the use of the fitting models. Apart from shedding light to the structural transition caused by the protein and tuned by the polysaccharide this work presents a system that may have great potential for controllable and enhanced encapsulation of globular proteins for nanodelivery applications.

Declaration of competing interest

The authors declare that they have no known competing financial interests or personal relationships that could have appeared to influence the work reported in this paper.

Acknowledgements

Authors wish to acknowledge the Budapest Neutron Centre (BNC) initiative to offer neutron beam time at the BNC Yellow Submarine SANS instrument as part of the BNC LENS beam time program (proposal number: BNC-LENS-663).

References

Almásy, L. 2021. New Measurement Control Software on the Yellow Submarine SANS Instrument at the Budapest Neutron Centre. *Journal of Surface Investigation: X-ray, Synchrotron and Neutron Techniques* 15: 527–531.

Barker, J.G.; Pedersen, J.S. 1995. Instrumental Smearing Effects in Radially Symmetric Small-Angle Neutron Scattering by Numerical and Analytical Methods. *Journal of Applied Crystallography* 28: 105–114.

Becker, A.L.; Henzler, K.; Welsch, N.; Ballauff, M.; Borisov, O. 2012. Proteins and polyelectrolytes: A charged relationship. *Current Opinion in Colloid & Interface Science* 17: 90–96.

Blom, A.; Warr, G.G.; Nelson, A. 2007. Structure of mixed DTAB/DDAB adsorbed layers on quartz: A neutron reflectometry and atomic force microscopy study. *Colloids and Surfaces A: Physicochemical and Engineering Aspects* 310: 1–8.

Bo, R.; Sun, Y.; Zhou, S.; Ou, N.; Gu, P.; Liu, Z.; et al. 2017. Simple nanoliposomes encapsulating Lycium barbarum polysaccharides as adjuvants improve humoral and cellular immunity in mice. *International journal of nanomedicine* 12: 6289–6301.

Comert, F.; Malanowski, A.J.; Azarikia, F.; Dubin, P.L. 2016. Coacervation and precipitation in polysaccharide–protein systems. *Soft Matter* 12: 4154–4161.

Eastoe, J.; Hetherington, K.J.; Dalton, J.S.; Sharpe, D.; Lu, J.R.; Heenan, R.K. 1997. Microemulsions with Didodecyldimethylammonium Bromide Studied by Neutron Contrast Variation. *Journal of Colloid and Interface Science* 190: 449–455.

Goodman, J.; Weare, J. 2010. Ensemble samplers with affine invariance. *Communications on Applied Mathematics and Computational Science* 5: 65–80.

Griffin, L.R.; Browning, K.L.; Truscott, C.L.; Clifton, L.A.; Webster, J.; Clarke, S.M. 2016. A comparison of didodecyldimethylammonium bromide adsorbed at mica/water and silica/water interfaces using neutron reflection. *Journal of Colloid and Interface Science* 478: 365–373.

Helfrich, W. 1986. Size distributions of vesicles : the role of the effective rigidity of membranes. *J. Phys. France* 47: 321–329.

Huang Changjin; Quinn David; Sadovsky Yoel; Suresh Subra; Hsia K. Jimmy. 2017. Formation and size distribution of self-assembled vesicles. *Proceedings of the National Academy of Sciences* 114: 2910–2915.

Jung H. T.; Coldren B.; Zasadzinski J. A.; Iampietro D. J.; Kaler E. W. 2001. The origins of stability of spontaneous vesicles. *Proceedings of the National Academy of Sciences* 98: 1353–1357.

462 Kaminski, G.A.T.; Sierakowski, M.R.; Pontarolo, R.; Santos, L.A. dos; Freitas, R.A. de. 2016.
463 Layer-by-layer polysaccharide-coated liposomes for sustained delivery of epidermal growth
464 factor. *Carbohydrate Polymers* 140: 129–135.
465 Komorowski, K.; Salditt, A.; Xu, Y.; Yavuz, H.; Brennich, M.; Jahn, R.; et al. 2018. Vesicle
466 Adhesion and Fusion Studied by Small-Angle X-Ray Scattering. *Biophysical Journal* 114: 1908–
467 1920.
468 Koo, B.I.; Kim, I.; Yang, M.Y.; Jo, S.D.; Koo, K.; Shin, S.Y.; et al. 2021. Protein-induced
469 metamorphosis of unilamellar lipid vesicles to multilamellar hybrid vesicles. *Journal of Controlled*
470 *Release* 331: 187–197.
471 van der Koog, L.; Gandek, T.B.; Nagelkerke, A. 2022. Liposomes and Extracellular Vesicles as
472 Drug Delivery Systems: A Comparison of Composition, Pharmacokinetics, and Functionalization.
473 *Advanced Healthcare Materials* 11: 2100639.
474 Kotlarchyk, M.; Stephens, R.B.; Huang, J.S. 1988. Study of Schultz distribution to model
475 polydispersity of microemulsion droplets. *The Journal of Physical Chemistry* 92: 1533–1538.
476 Kunz, W.; Testard, F.; Zemb, T. 2009. Correspondence between Curvature, Packing Parameter,
477 and Hydrophilic−Lipophilic Deviation Scales around the Phase-Inversion Temperature. *Langmuir*
478 25: 112–115.
479 Lee, J.-H.; Agarwal, V.; Bose, A.; Payne, G.F.; Raghavan, S.R. 2006. Transition from Unilamellar
480 to Bilamellar Vesicles Induced by an Amphiphilic Biopolymer. *Phys. Rev. Lett.* 96: 048102.
481 Len, A.; Almásy, L. 2019. Small Angle Neutron Scattering. In: Füzi, J.; Len, A.; Bajnok, K. (Eds.),
482 *Research Instruments at the Budapest Neutron Centre*, Hungarian Academy of Sciences,
483 Budapest, p.11–27.

Lenormand, H.; Vincent, J.-C. 2011. pH effects on the hyaluronan hydrolysis catalysed by hyaluronidase in the presence of proteins: Part II. The electrostatic hyaluronan – Protein complexes. *Carbohydrate Polymers* 85: 303–311.

Liu, Z.; Dong, C.; Wang, X.; Wang, H.; Li, W.; Tan, J.; et al. 2014. Self-Assembled Biodegradable Protein–Polymer Vesicle as a Tumor-Targeted Nanocarrier. *ACS Applied Materials & Interfaces* 6: 2393–2400.

Marques, E.F.; Regev, O.; Khan, A.; Lindman, B. 2003. Self-organization of double-chained and pseudodouble-chained surfactants: counterion and geometry effects. *Advances in Colloid and Interface Science* 100–102: 83–104.

Mehan, S.; Chinchalikar, A.J.; Kumar, S.; Aswal, V.K.; Schweins, R. 2013. Small-Angle Neutron Scattering Study of Structure and Interaction of Nanoparticle, Protein, and Surfactant Complexes. *Langmuir* 29: 11290–11299.

Nayerhoda, R.; Hill, A.; Pfeifer, B.A. 2021. Liposomal Dual Delivery of Both Polysaccharide and Protein Antigens. In: Pfeifer, B.A.; Hill, A. (Eds.), *Vaccine Delivery Technology: Methods and Protocols*, Springer US, New York, NY, p.477–487.

Papagiannopoulos, A. 2018. Bovine serum albumin interactions with cationic surfactant vesicles decorated by a low-molar-mass polysaccharide. *Colloids and Surfaces A: Physicochemical and Engineering Aspects* 537: 495–501.

Papagiannopoulos, A.; Vlassi, E.; Pispas, S.; Jafta, C.J. 2017. Tuning the solution organization of cationic polymers through interactions with bovine serum albumin. *Phys. Chem. Chem. Phys.* 19: 18471–18480.

505 Papagiannopoulos, A.; Pippa, N.; Demetzos, C.; Pispas, S.; Radulescu, A. 2021a. Lamellarity and
506 size distributions in mixed DPPC/amphiphilic poly(2-oxazoline) gradient copolymer vesicles and
507 their temperature response. *Chemistry and Physics of Lipids* 234: 105008.
508 Papagiannopoulos, A.; Pippa, N.; Demetzos, C.; Pispas, S.; Radulescu, A. 2021b. Formation of
509 Uni-Lamellar Vesicles in Mixtures of DPPC with PEO-b-PCL Amphiphilic Diblock Copolymers.
510 *Polymers* 13.
511 Pedersen, J.S. 1997. Analysis of small-angle scattering data from colloids and polymer solutions:
512 modeling and least-squares fitting. *Advances in Colloid and Interface Science* 70: 171–210.
513 Pistone, S.; Rykke, M.; Smistad, G.; Hiorth, M. 2017. Polysaccharide-coated liposomal
514 formulations for dental targeting. *International Journal of Pharmaceutics* 516: 106–115.
515 Radulescu, A.; Székely, N.K.; Polachowski, S.; Leyendecker, M.; Amann, M.; Buitenhuis, J.; et
516 al. 2015. Tuning the instrument resolution using chopper and time of flight at the small-angle
517 neutron scattering diffractometer KWS-2. *Journal of Applied Crystallography* 48: 1849–1859.
518 Regev, O.; Khan, A. 1994. Vesicle — lamellar transition events in DDAB-water solution. *Trends*
519 *in Colloid and Interface Science VIII*: 298–301.
520 Rodrigues-Jesus, M.J.; Fotoran, W.L.; Cardoso, R.M.; Araki, K.; Wunderlich, G.; Ferreira, L.C.S.
521 2019. Nano-multilamellar lipid vesicles (NMVs) enhance protective antibody responses against
522 Shiga toxin (Stx2a) produced by enterohemorrhagic Escherichia coli strains (EHEC). *Brazilian*
523 *Journal of Microbiology* 50: 67–77.
524 Román-Aguirre, M.; Leyva-Porras, C.; Cruz-Alcantar, P.; Aguilar-Elguézabal, A.; Saavedra-Leos,
525 M.Z. 2020. Comparison of Polysaccharides as Coatings for Quercetin-Loaded Liposomes (QLL)
526 and Their Effect as Antioxidants on Radical Scavenging Activity. *Polymers* 12.

Ruggeri, F.; Zhang, F.; Lind, T.; Bruce, E.D.; Lau, B.L.T.; Cárdenas, M. 2013. Non-specific interactions between soluble proteins and lipids induce irreversible changes in the properties of lipid bilayers. *Soft Matter* 9: 4219–4226.

Ruttala, H.B.; Ramasamy, T.; Gupta, B.; Choi, H.-G.; Yong, C.S.; Kim, J.O. 2017. Multiple polysaccharide–drug complex-loaded liposomes: A unique strategy in drug loading and cancer targeting. *Carbohydrate Polymers* 173: 57–66.

Salim, M.; Minamikawa, H.; Sugimura, A.; Hashim, R. 2014. Amphiphilic designer nano-carriers for controlled release: from drug delivery to diagnostics. *MedChemComm* 5: 1602–1618.

Stovgaard, K.; Andreetta, C.; Ferkinghoff-Borg, J.; Hamelryck, T. 2010. Calculation of accurate small angle X-ray scattering curves from coarse-grained protein models. *BMC bioinformatics* 11: 429.

Sun, H.; Yang, L.; Thompson, M.P.; Schara, S.; Cao, W.; Choi, W.; et al. 2019. Recent Advances in Amphiphilic Polymer–Oligonucleotide Nanomaterials via Living/Controlled Polymerization Technologies. *Bioconjugate Chemistry* 30: 1889–1904.

Vanderbilt, D.; Louie, S.G. 1984. A Monte carlo simulated annealing approach to optimization over continuous variables. *Journal of Computational Physics* 56: 259–271.

Winslow, S.W.; Shcherbakov-Wu, W.; Liu, Y.; Tisdale, W.A.; Swan, J.W. 2019. Characterization of colloidal nanocrystal surface structure using small angle neutron scattering and efficient Bayesian parameter estimation. *The Journal of Chemical Physics* 150: 244702.

Forthcoming. https://nl.mathworks.com/matlabcentral/fileexchange/49567-cornerplot. .